

RESEARCH

Open Access



Experimental and Numerical Analysis of the Ribbed Reinforced Concrete Fracture Behavior Based on the Mesoscale FE Model

Zhanliang Wang¹, Wei Zhang^{1*}  and Yiqun Huang¹

Abstract

This study presented a meso-model for the fracture analysis of the reinforced concrete (RC) structure. A modeling method of RC meso-structure was proposed, and the rebars were allowed to separate from the concrete. The model was built using the cohesive zone model (CZM). The zero-thickness cohesive elements were adopted to characterize the mechanical behavior of potential fracture surfaces and rebar–concrete interfaces. The constitutive model for concrete was developed by considering the damage relation and friction effect, and the corresponding constitutive model for the rebar–concrete interface (especially ribbed rebar) was developed by considering the influence of normal separation on the tangential bond–slip relation. To validate the proposed meso-model, a series of ribbed RC beams with an initial notch was designed and tested by four-point bending loading to obtain different fracture patterns. Through comparison, the developed RC meso-model was validated to simulate the RC structure's fracture behavior appropriately. The influence of the rebar–concrete interface constitutive model on the simulation results was investigated. The investigation results indicate that neglecting normal separation would result in an overestimation of the structure's stiffness and bearing capacity (the peak load was overestimated by more than 10%). Finally, an analysis was conducted on the energy consumption during the failure process of the RC beams. It was found that the proportion of energy consumption during tensile failure of the beam decreased from approximately 86% to 89% in the early stage to approximately 43% to 52% in the later stage, indicating a transition in the beam's failure mode from tensile failure to shear failure.

Keywords Mesoscale, Ribbed RC beam, Cohesive element, Crack propagation, Energy analysis

1 Introduction

Reinforced concrete is one of the world's most widely used building materials due to its high tensile and compressive strength, low cost, and convenient construction. To better design reinforced concrete structures, many relevant studies have been carried out in recent years

(Deng et al., 2020; Fan et al., 2022; Jeong et al., 2017; Li & Wu, 2018; Murthy et al., 2018).

To investigate the fracture behavior of reinforced concrete structure at a mesoscopic scale, a mature and effective numerical concrete meso-model should be established first, which can characterize the configuration, including aggregates, cement matrix, and interface transition zone (ITZ). Two methods were developed to rebuild the concrete structure at a mesoscopic scale for studying the fracture behavior and mechanical properties. One is to generate aggregates/pores by throwing polygons randomly (Huang & Hu, 2019; Naderi & Zhang, 2021; Shen et al., 2015), and the other is to restructure internal components of concrete by tomography

Journal information: ISSN 1976-0485 / eISSN 2234-1315

*Correspondence:

Wei Zhang

zhangwei621@gmail.com

¹ School of Civil Engineering, Fujian University of Technology, Fuzhou 350118, China

(Bernachy-Barbe & Bary, 2019; Yang et al., 2017). In addition, many numerical methods have been presented to analyze the rebuilt concrete model, including the traditional finite element method (FEM) adopting continuing solid elements (Liu et al., 2019; Pedersen et al., 2013; Shen et al., 2015) or lattice elements (Grassl, 2022; Karavelić et al., 2019; Sun et al., 2020), the extended finite element method (XFEM) (Chaudhuri, 2013; Chen et al., 2020; Roth et al., 2015; Xia et al., 2021), and the cohesive zone model (CZM) based on the application of the coherent element (De Maio et al., 2022; Huang & Hu, 2019; Huang et al., 2022; López et al., 2008a, 2008b; Wang et al., 2015). Especially the CZM method is one of the most advantageous numerical methods to simulate interfacial mechanical behavior.

Another critical aspect of simulating reinforced concrete is the bond model between the concrete and rebars. Previous works have presented the bond–slip models at three scales (Cox & Herrmann, 1998): (a) rib scale, in which scale the geometry of the bar’s surface is considered explicitly (Jin et al., 2020; Liu et al., 2022). However, this model was rarely used due to the huge mesh quantity and difficulty simulating the large slip. (b) Bar scale, the mechanical interaction of the ribs is homogenized as an interface phenomenon (Li & Wu, 2018; Syroka-Korol & Tejchman, 2014; Syroka-Korol et al., 2014). (c) Member scale, a discrete, embedded, or smeared model, is usually used to describe the reinforcement in this scale. Due to the high efficiency of the computation, the member-scale model was widely used in previous research (Du et al., 2013; Murthy et al., 2018; Ooi & Yang, 2011). However, due to the bond–slip relation of the rebar–concrete interface being ignored in the member-scale model, the calculation accuracy is hard to control in some conditions.

In this paper, an RC meso-model was proposed based on the CZM. The zero-thickness cohesive elements were used to represent the ITZ, potential fracture surfaces, and the rebar–concrete interface. The corresponding constitutive models were developed to characterize the

propagation of concrete cracks and the bond–slip relation of the rebar–concrete interface. Four-point bending (FPB) experiments were designed and carried out to validate the proposed meso-model. Finally, the influence of the rebar–concrete interfacial constitutive model on the simulation result was also investigated.

2 Meso-modelling of the RC Structure

In the simulation of RC structures, two aspects should be concerned: the fracture of concrete and the bond–slip behavior of the rebar–concrete interface. In this study, a two-dimension (2D) meso-model was proposed by considering these two critical aspects.

2.1 Meso-modelling of Concrete

The generation method in the previous work (Huang & Hu, 2019; Shen et al., 2015) was adopted to build up the concrete meso-structure. As shown in Fig. 1, the concrete meso-model consists of mortar, aggregate, ITZ, and potential fracture surfaces. The mortar and aggregate are represented by solid elements (triangular element in this study), and zero-thickness cohesive elements represent ITZ and potential fracture surfaces. Based on the concrete meso-model, the area where the rebars embed is pre-marked for the insertion of rebars and the corresponding concrete–rebar interface, as shown in Fig. 1a.

2.2 Modelling of Rebars and Rebar–Concrete Interfaces

Fig. 2 shows the modeling of the rebars and rebar–concrete interfaces. Based on the generated concrete meso-model, the rebars were generated by copying the node and element information of the pre-marked area in concrete. Besides, the rebars were connected with concrete by zero-thickness cohesive elements, which were used to characterize the traction–separation and bond–slip relations of the rebar–concrete interfaces.

In summary, the steps to build up the RC meso-model can be given as follows:

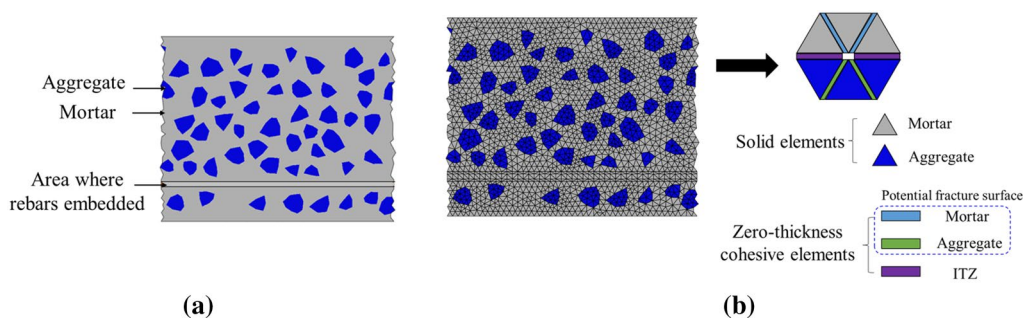


Fig. 1 Meso-model of concrete **a** consists of concrete meso-model **b** elements of the meso-model

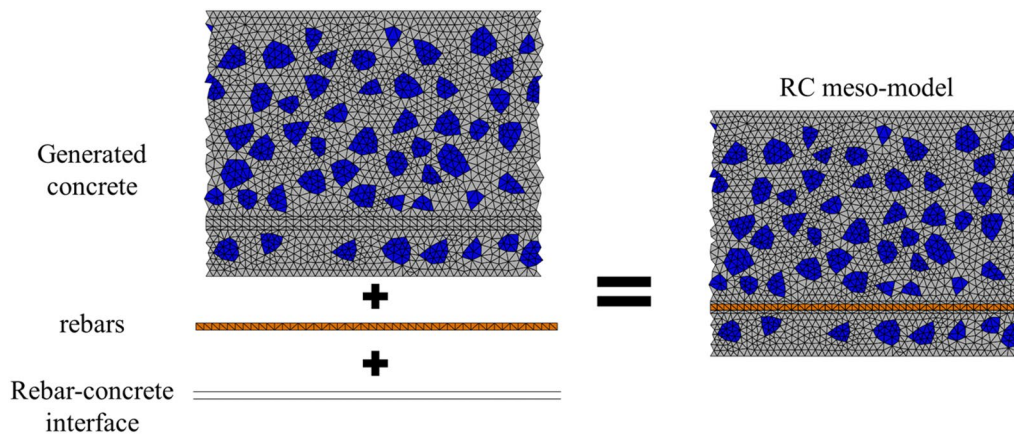


Fig. 2 Modelling of rebars and rebar–concrete interfaces

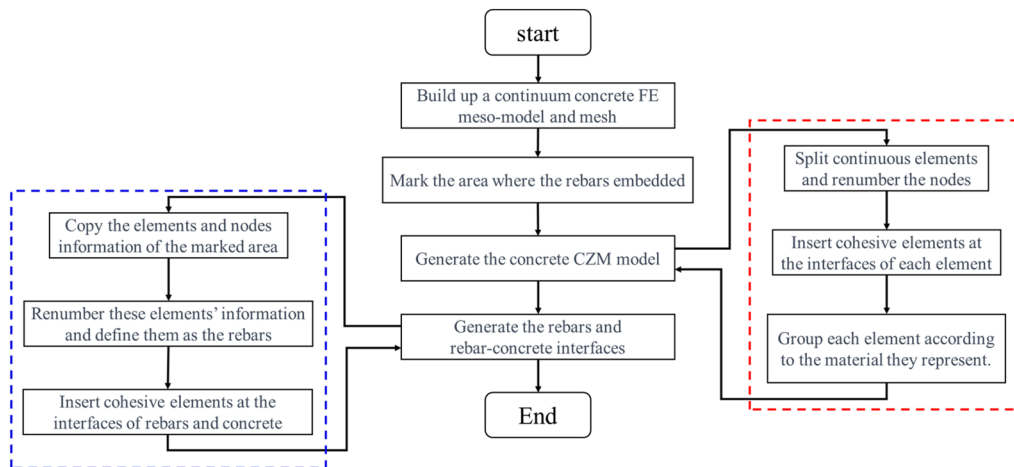


Fig. 3 Flowchart for generating the mesoscale RC model

Step 1: Generate the concrete meso-model, and pre-mark the area where the rebars are embedded.

Step 2: Generate the rebars by copying the mesh information of the area pre-marked in step 1.

Step 3: Generate the rebar–concrete interface (cohesive elements) according to the rebars and concrete mesh information.

The brief flowchart for generating the mesoscale reinforced concrete (RC) model is presented in Fig. 3.

Finally, the element composition of the RC meso-model is shown in Fig. 4. The solid elements were used to simulate the mortar, aggregate, and rebars. The zero-thickness cohesive elements were used to simulate the potential fracture surfaces and rebar–concrete interfaces. Especially the cohesive elements were divided into four kinds according to the objects they simulate: (1) CE_MOR for the potential fracture surfaces of mortar; (2) CE_ITZ for the ITZ between aggregate and mortar; (3) CE_AGG for the potential fracture surfaces of aggregate; (4) CE_BOND for the rebar–concrete interface.

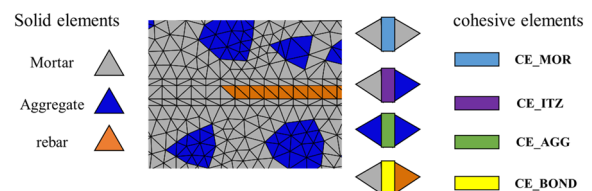


Fig. 4 Element composition of the RC meso-model

2.3 Constitutive Model of Different Components

2.3.1 Constitutive Model of Concrete Potential Fracture Surfaces

(1) Mixed-mode damage relation

The constitutive model of concrete potential fracture surfaces combined the mixed-mode damage relation and friction effect. The bilinear damage relation was adopted (Huang & Hu, 2019), as shown in Fig. 5, and the damage relation in single-mode condition can be expressed as follows:

$$t_n = \begin{cases} k_n \delta_n & \delta_n \leq \delta_{n0} \\ (1 - D)k_n \delta_n & \delta_{n0} < \delta_n < \delta_{nf} \\ 0 & \delta_n > \delta_{nf} \end{cases}, \quad t_s = \begin{cases} k_s \delta_s & |\delta_s| \leq \delta_{s0} \\ (1 - D)k_s \delta_s & \delta_{s0} < |\delta_s| < \delta_{sf} \\ 0 & |\delta_s| > \delta_{sf} \end{cases} \quad (1)$$

where t_n is the normal stress; t_s is the shear stress; k_n and k_s are the normal and tangential initial stiffness, respectively; δ_n and δ_s are the normal and tangential displacement, respectively; δ_{n0} is the normal damage initial displacement; δ_{nf} is the normal failure displacement; δ_{s0} is the tangential damage initial displacement; δ_{sf} is the tangential failure displacement. D is the damage factor, which can be calculated in the single-mode condition:

$$D = \frac{(\delta_n - \delta_{n0})\delta_{nf}}{(\delta_{nf} - \delta_{n0})\delta_n} \text{ (Normal direction),} \quad (2)$$

$$D = \frac{(|\delta_s| - \delta_{s0})\delta_{sf}}{(\delta_{sf} - \delta_{s0})|\delta_s|} \text{ (Tangential direction).}$$

In the mixed-mode condition, the quadric criterion was adopted to define the initiation of the damage process:

$$\left(\frac{t_n}{t_{n0}}\right)^2 + \left(\frac{t_s}{t_{s0}}\right)^2 = 1, \quad (3)$$

where t_{n0} is the tensile strength; t_{s0} is the shear strength.

The energy consumption in the mixed mode is assumed to follow the PL criterion, which can be given as follows:

$$\frac{G_n^r}{G_n} + \frac{G_s^r}{G_s} = 1, \quad (4)$$

where G_n and G_s are the fracture energy in the normal direction and tangential direction, respectively, which is the area under the curve in Fig. 4; G_n^r and G_s^r are the normal and tangential energy release rate in the mixed-mode condition, which can be expressed as follows:

$$G_n^r = \frac{k_n \delta_{n0}^r \delta_{nf}^r}{2}, G_s^r = \frac{k_s \delta_{s0}^r \delta_{sf}^r}{2}, \quad (5)$$

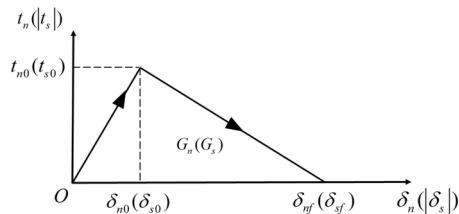


Fig. 5 Bilinear damage model in the single-mode condition

where δ_{n0}^r and δ_{s0}^r are the relatively normal and tangential damage initial displacement; δ_{nf}^r and δ_{sf}^r are the relatively normal and tangential failure displacement.

Assuming that the loading path is monotonous, according to the geometry relation in Fig. 4 and Eqs. (3, 4, 5), the relative damage initial displacements and relative failure displacements can be given as follows:

$$\begin{cases} \delta_{n0}^r = \frac{\delta_n \delta_{n0} \delta_{s0}}{\sqrt{\delta_{n0}^2 \delta_s^2 + \delta_n^2 \delta_{s0}^2}} \\ \delta_{s0}^r = \frac{|\delta_s| \delta_{n0} \delta_{s0}}{\sqrt{\delta_{n0}^2 \delta_s^2 + \delta_n^2 \delta_{s0}^2}} \end{cases}, \quad \begin{cases} \delta_{nf}^r = \frac{2\delta_{n0}^r G_n G_s}{k_n \delta_{n0}^r{}^2 G_s + k_s \delta_{s0}^r{}^2 G_n} \\ \delta_{sf}^r = \frac{2\delta_{s0}^r G_n G_s}{k_n \delta_{n0}^r{}^2 G_s + k_s \delta_{s0}^r{}^2 G_n} \end{cases}. \quad (6)$$

Based on the parameters obtained above, define the total displacement $\delta = \sqrt{\delta_n^2 + \delta_s^2}$, total damage initial displacement $\delta_0 = \sqrt{\delta_{n0}^r{}^2 + \delta_{s0}^r{}^2}$, and total failure displacement $\delta_f = \sqrt{\delta_{nf}^r{}^2 + \delta_{sf}^r{}^2}$. The damage factor in the mixed-mode condition can be expressed as follows:

$$D = \frac{(\delta - \delta_0)\delta_f}{(\delta_f - \delta_0)\delta}. \quad (7)$$

It should be noticed that the equations given above are only available in the crack-opening condition ($\delta_n > 0$). In the crack-closing condition ($\delta_n < 0$), the damage factor is calculated by assuming that the crack follows single-mode shear damage relation (Eq. (1)).

(2) Friction effect

When the potential fracture surfaces initiate the damage, which means the cracks begin to expand, the friction stress will occur if the crack is under compression. Thus, the friction stress T_f can be calculated in the condition that the relative slide is not happening:

$$T_f = k_s (\delta_s - \delta_s^{slide}) \left(k_s (\delta_s - \delta_s^{slide}) \leq T_{fmax} \right), \quad (8)$$

where δ_s^{slide} is the slide displacement which has been generated; T_{fmax} is the maximum friction stress, which can be given as follows:

$$T_{fmax} = f \langle -k_n \delta_n \rangle. \quad (9)$$

When the relative slide occurs, the friction stress and the corresponding slide displacement should be calculated as follows:

$$\begin{cases} T_f = f \langle -k_n \delta_n \rangle \frac{\delta_s - \delta_s^{slide}}{|\delta_s - \delta_s^{slide}|} & (k_s |\delta_s - \delta_s^{slide}| > T_{f,max}) \\ \delta_s^{slide*} = \delta_s - \frac{T_f}{k_s} \end{cases} \quad (10)$$

(3) Total stresses calculation

Finally, according to the mixed-mode damage relation and the friction effect, the stresses can be expressed as follows:

$$\begin{aligned} t_n &= \begin{cases} k_n \delta_n & \delta \leq \delta_0 \\ (1-D)k_n \delta_n & \delta_0 < \delta < \delta_f \\ 0 & \delta > \delta_f \end{cases} \\ t_s &= \begin{cases} k_s \delta_s & |\delta_s| \leq \delta_{s0} \\ (1-D)k_s \delta_s + D \cdot T_f & \delta_{s0} < |\delta_s| < \delta_{sf} \\ D \cdot T_f & |\delta_s| \geq \delta_{sf} \end{cases} \end{aligned} \quad (11)$$

2.3.2 Constitutive Model of Rebar–Concrete Interfaces

In this study, the constitutive model proposed in the previous research (Den Syroka-Korol et al., 2014; Uijl & Bigaj, 1996) was adopted and modified to characterize the bond–slip relation of the ribbed rebar–concrete interface. In this constitutive model, the stress transfer mechanism of the interface can be equivalent to the form, as shown in Fig. 6b, and the steel rebar is equal to a

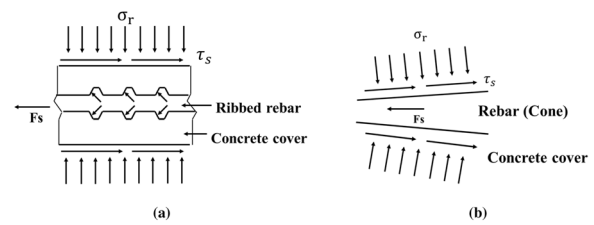


Fig. 6 Equivalence of the rebar–concrete interfacial stress transfer mechanism: **a** realistic stress transfer mechanism; **b** equivalent stress transfer mechanism

cone. Thus, the mechanical interaction of the interface, as shown in Fig. 6a, can be simplified to the normal stress σ_r and shear stress τ_s , which can be easily calculated.

In the equivalent model, the bond–slip relation is mainly reflected by the normal stress σ_r , and the normal stress distribution along the concrete cover can be seen in Fig. 7a. As the relative slip of the rebar, the rebar would squeeze the concrete cover and cause it to crack, which leads to a decrease in the normal stress, as shown in Fig. 7b. The bond–slip process of the rebar can be divided into three stages: (1) the rebar slips and squeezes the concrete cover, and the concrete keeps complete; (2) with the concrete damage and cracking, the interaction between the rebar and concrete decreases; (3) the cracks of the concrete cover propagate thoroughly, and the interaction between the rebar and concrete keeps stable.

Thus, the normal stress of the interface $\sigma_r(rs)$ can be calculated through the formulations as follows:

$$\sigma_r(rs) = \begin{cases} \sigma_{r,max} \frac{k\eta - \eta^2}{1 + (k-2)\eta} & (0 \leq \varepsilon_r(rs) \leq \varepsilon_{r,max}) \\ \sigma_{r,max} \left(1 - \frac{1-\psi}{\varepsilon_{r,res} - \varepsilon_{r,max}} (\varepsilon_r(rs) - \varepsilon_{r,max}) \right) & (\varepsilon_{r,max} \leq \varepsilon_r(rs) \leq \varepsilon_{r,res}) \\ \psi \cdot \sigma_{r,max} & (\varepsilon_{r,res} \leq \varepsilon_r(rs)) \end{cases} \quad (12)$$

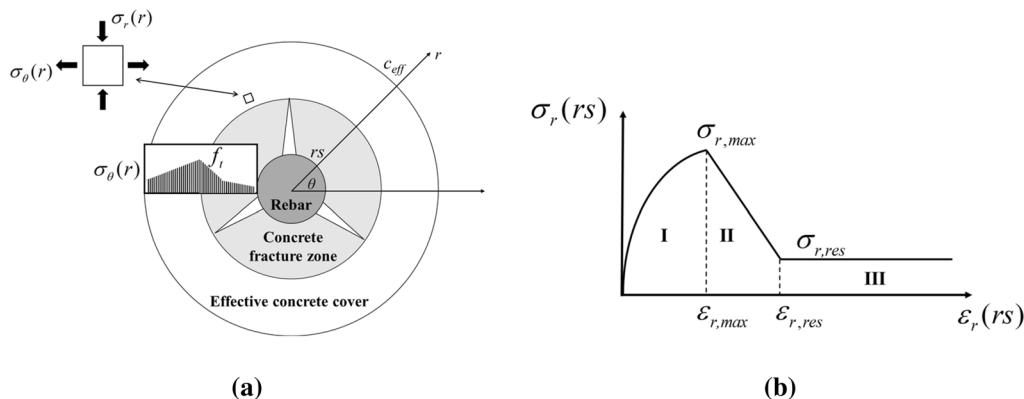


Fig. 7 Mechanism of the interaction between rebar and concrete: **a** concrete cover cracking mechanism; **b** stress–strain relation of the interface in the normal direction

where $\sigma_{r,max}$ is the maximum normal compression stress; k and η are the computation parameters; ψ is the factor of residual stress; $\varepsilon_r(rs)$ is the normal strain of the concrete cover at the interface; $\varepsilon_{r,max}$ and $\varepsilon_{r,res}$ are the strain values corresponding to different stages as shown in Fig. 6b.

In Eq. (12), the maximum normal compression stress $\sigma_{r,max}$ and the corresponding strain $\varepsilon_{r,max}$ can be expressed as follows:

$$\sigma_{r,max} = 2f_t \left(\frac{c_{eff}}{\phi} \right)^{0.88}, \varepsilon_{r,max} = 4.2 \frac{f_t}{E} \left(\frac{c_{eff}}{\phi} \right)^{1.08}, \tag{13}$$

where f_t is the tensile strength of concrete; c_{eff} is the effective thickness of the concrete cover; ϕ is the diameter of the rebar; E is the elastic modulus of concrete.

Besides, the computation parameters k and η in Eq. (12) can be given as follows:

$$k = \frac{E_r \cdot \varepsilon_{r,max}}{\sigma_{r,max}}, \eta = \frac{\varepsilon_r(rs)}{\varepsilon_{r,max}}, \tag{14}$$

where E_r is the radial stiffness of the concrete, which can be expressed as follows:

$$E_r = \frac{E}{\left(\frac{(c_{eff} + \phi/2)^2 + \phi^2/4}{(c_{eff} + \phi/2)^2 - \phi^2/4} + \mu \right)} \tag{15}$$

where μ is the Poisson's ratio of concrete.

The strain value $\varepsilon_{r,res}$ corresponding to the residual stress in Eq. (12) can also be given as follows:

$$\sigma_r(rs) = D_2 \cdot \begin{cases} \sigma_{r,max} \frac{k\eta - \eta^2}{1 + (k-2)\eta} & (0 \leq \varepsilon_r(rs) \leq \varepsilon_{r,max}) \\ \sigma_{r,max} \left(1 - \frac{1-\psi}{\varepsilon_{r,res} - \varepsilon_{r,max}} (\varepsilon_r(rs) - \varepsilon_{r,max}) \right) & (\varepsilon_{r,max} \leq \varepsilon_r(rs) \leq \varepsilon_{r,res}) \\ \psi \cdot \sigma_{r,max} & (\varepsilon_{r,res} \leq \varepsilon_r(rs)) \end{cases} \tag{21}$$

$$\varepsilon_{r,res} = \frac{f_t}{E} \left(\frac{2c_{eff} + c_0}{\phi} \right), \tag{16}$$

where c_0 is an empirical parameter.

From the aspect of engineering safety, the splitting fracture rather than the pulling-out fracture was chosen as the main fracture mode of the rebar–concrete interface. Thus, the relation (Den Syroka-Korol et al., 2014; Uijl & Bigaj, 1996) between the slip displacement s and the strain value $\varepsilon_r(rs)$ can be given as follows:

$$\varepsilon_r(rs) = \frac{2s}{\phi} \tan \nu_b, \tag{17}$$

where ν_b is the angle of the cone as shown in Fig. 5b, which can be calculated as follows:

$$\nu_b [^\circ] = 0.1f_c [\text{MPa}], \tag{18}$$

where f_c is the compression strength of concrete.

Finally, the shear stress τ_s can be calculated according to the normal stress of the interface (Den Syroka-Korol et al., 2014; Uijl & Bigaj, 1996):

$$\tau_s = \sigma_r(rs). \tag{19}$$

It should be noted that the formulas listed above can only be applied in the pure shear condition. However, in most conditions, the failure of the rebar–concrete interface is the mixed-mode fracture, which means the interface can also be separated in the normal direction, as shown in Fig. 8. In this model, the normal separation behavior of the interface was assumed to follow the single-mode damage relation define in Eq. (1), and the weakening parameter D_2 was defined to characterize the weakening effect of normal separation on the tangential bond–slip relation:

$$D_2 = \begin{cases} 1 & \delta_n \leq 0 \\ (h_l - \delta_n)/h_l & 0 \leq \delta_n \leq h_l \\ 0 & \delta_n \geq h_l \end{cases}, \tag{20}$$

where h_l is the height of the rib as shown in Fig. 7

Finally, the bond–slip relation can be modified as follows:

3 Four-Point Bending Experiments of Ribbed RC Beams Without Stirrups

3.1 Geometry and Loading Scheme

To validate the accuracy of the proposed RC meso-model, a series of four-point bending (FPB) RC beams without stirrups were designed (Syroka-Korol & Tejchman, 2014; Syroka-Korol et al., 2014). The size of the beam is length \times width \times height = 1500 mm \times 200 mm \times 200 mm. Four

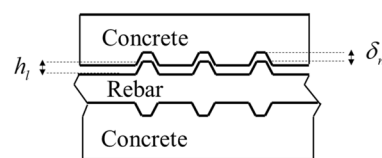


Fig. 8 Normal separation of the rebar–concrete interface

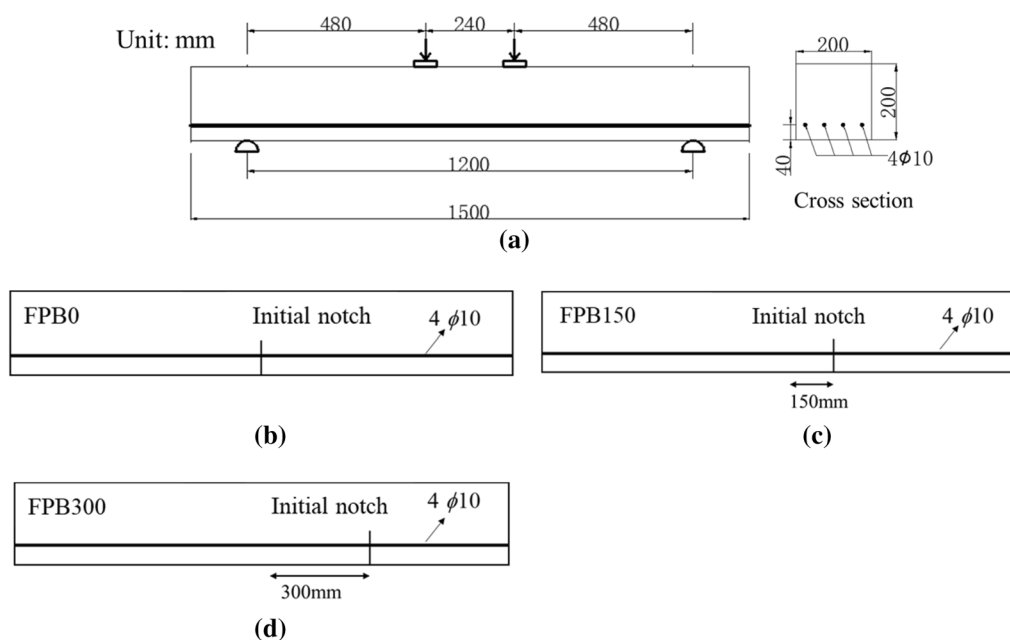


Fig. 9 Geometry and loading scheme of the ribbed RC beams: **a** FPBS; **b** FPB0; **c** FPB150; **d** FPB300

ribbed rebars with 10 mm diameter were embedded at the bottom of the beam with 50 mm spacing. The concrete cover was set to 40 mm. The geometry of the RC beam is shown in Fig. 9a, and the beams in this group were called FPBS. Besides, three groups of beams with different initial notches were designed to obtain more fracture patterns, as shown in Fig. 9b–d. The length of the initial notches was set to 80 mm. The distances from the initial notches to the middle of the beams were set to 0 mm, 150 mm, and 300 mm, respectively, and the corresponding beams were called FPB0, FPB150, and FPB300, respectively. The design details of the test specimens are listed in Table 1.

In every group, four specimens were cast to eliminate the random errors caused by the materials and experiments. The design strength of the concrete was C35, and the mix ratio of the concrete is cement:sand:aggregate:water = 1: 0.85: 1.98: 0. 43. Besides, the crushed stone with a particle size ranging from 5 to 20 mm and P.O42.5 grade

cement were adopted to cast the concrete. The preparation of test can be seen in Fig. 10. Through the material property tests, the standard compressive strength and the elastic modulus of concrete were about 40 MPa and 30 GPa, respectively. The yield strength and the elastic modulus of the HRB400 steel rebar were about 400 MPa and 200 GPa, respectively.

The loading scheme of the test beams is shown in Fig. 11. The distance between the two supports was set to 1200 mm, and the length of the pure bending section was set to 240 mm. To obtain the distribution of the deflection, 5 LVDT displacement gauges were uniformly placed under the beam with 200 mm spacing. Also, a force sensor with 300kN was used to record the loading force. During the test, force-controlled loading is used before the test specimen reaches peak load, while displacement-controlled loading is used afterwards, and the loading rate is controlled at about 1kN/min.

Table 1 Design details of the specimens

Specimen	Amount	Steel rebars	Concrete	Initial notch length	Location of the initial notch
FPBS	3	4ϕ10	C35	80 mm	–
FPB0	3				Mid-span
FPB150	3				150 mm from mid-span
FPB300	3				300 mm from mid-span

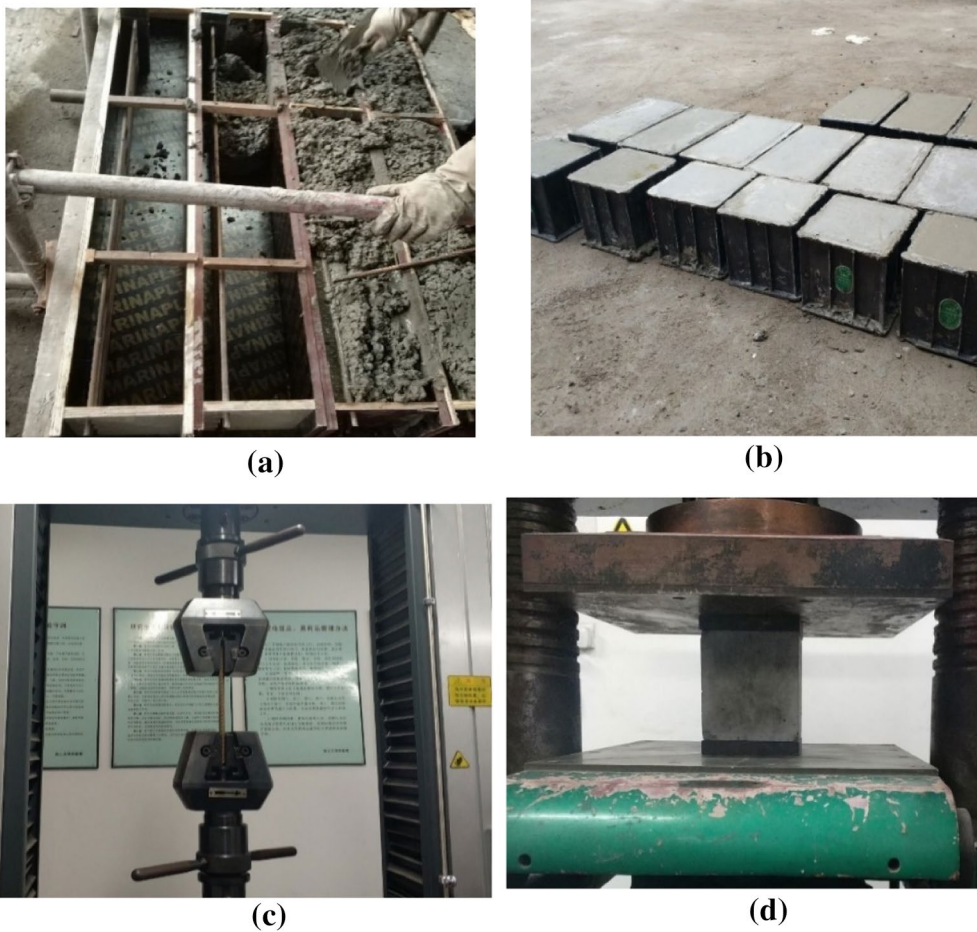


Fig. 10 Preparation of the test: **a** casting of beam specimens; **b** casting of standard cubic specimens; **c** tensile testing of steel reinforcements; **d** compressive strength testing of concrete

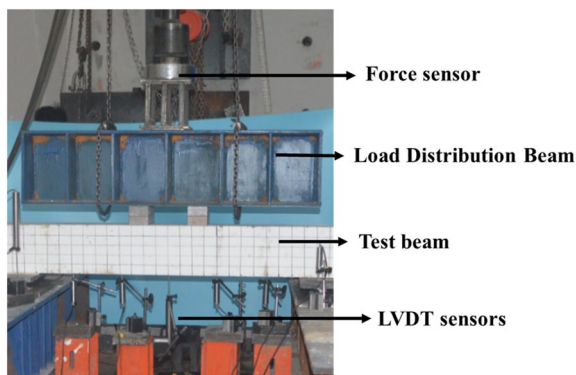


Fig. 11 Testing method of the RC beams

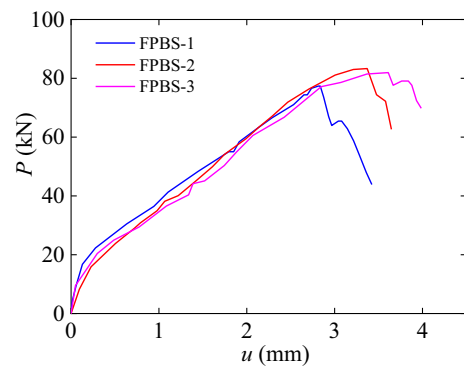


Fig. 12 $P-u$ curves of the beams in group FPBS

3.2 Experimental Results

The load vs. midspan displacement curves ($P-u$ curves) of the beams in group FPBS are shown in Fig. 12. The results of the beams show a typical brittle characterization. The

loading force increased linearly with the increase of midspan displacement at the beginning of the loading process. When the force reached about 20–25kN, the cracks occurred in the bottom of the concrete and kept propagating, and an inflection point was also observed in the

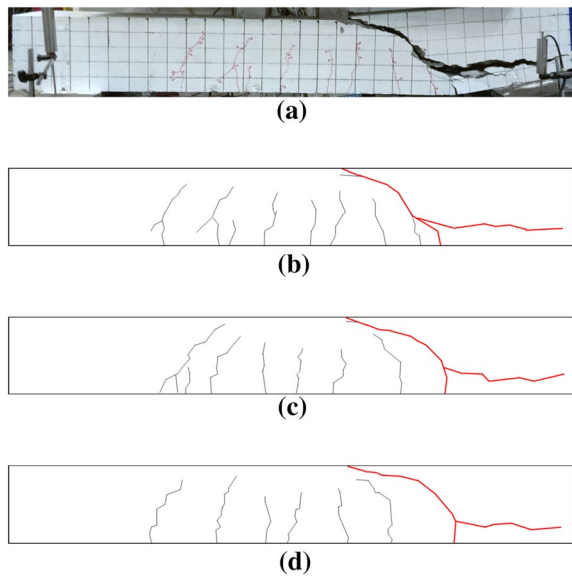


Fig. 13 Distribution of cracks in group FPBS: **a–b** experimental result of FPBS-1; **c** FPBS-2; **d** FPBS-3

corresponding $P-u$ curve. Finally, when the loading force reached peak value (about 80kN), the beam suddenly lost its bearing capacity with a major diagonal crack penetrating the specimens, as shown in Fig. 13.

Fig. 13 shows the final distribution of cracks in the group FPBS. To conveniently compare the crack distribution of the RC beams, all the main cracks were set on the right side. All beams failed with a main crack propagating diagonally in the shear section and penetrating the beam, and these main cracks have been marked in red, as shown in Fig. 10b–c.

The load–displacement curves of the RC beams with initial notches are shown in Fig. 14. It can be seen that the location of the initial notch significantly influences the mechanical behavior of the RC beams. When the initial notch moves from the middle to the side of the beam, the failure mode changes from a brittle fracture into a ductile fracture. This result is because the initial notch would change the location and propagation of the main crack, as shown in Fig. 15d.

Fig. 15 shows the final distribution of the cracks in different experimental groups. To conveniently compare the crack distribution of the RC beams, all the main cracks

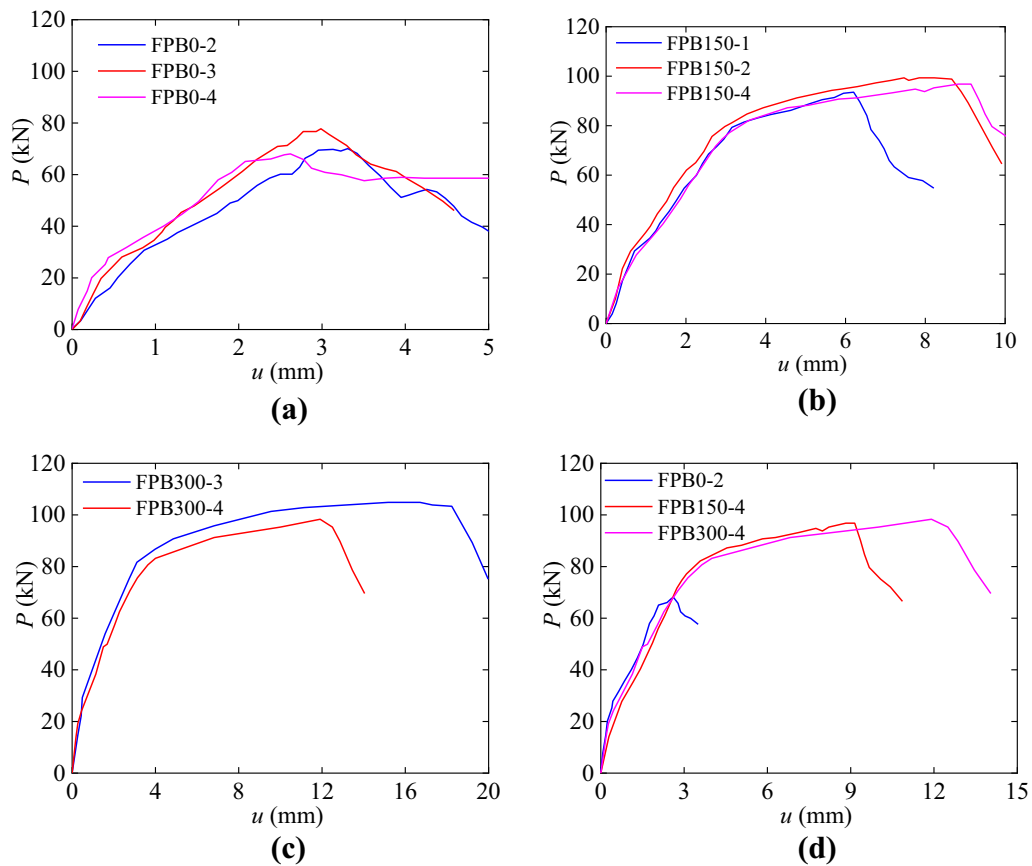


Fig. 14 $P-u$ curves of the beams with an initial notch: **a** FPB0; **b** FPB150; **c** FPB300; **d** comparison between different groups

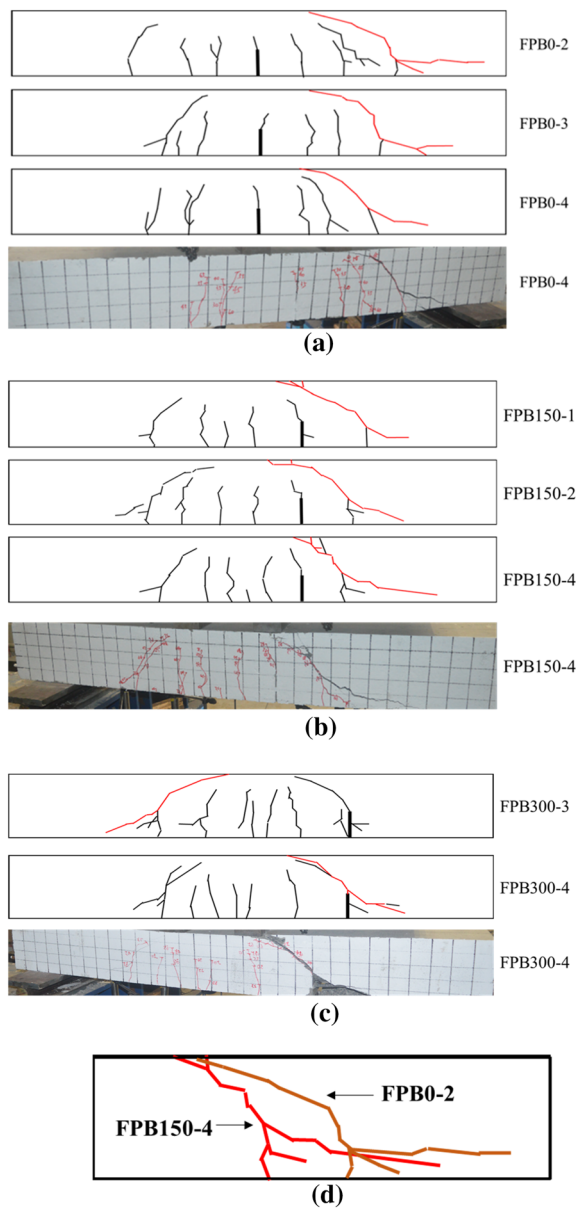


Fig. 15 Distribution of the cracks in different experimental groups: **a** FPB0; **b** FPB150; **c** FPB300; **d** comparison between different groups

were set on the right side. All the RC beams in different groups show a similar fracture pattern. The cracks initiated first in the pure-bending section of the beam and propagated. With the continued loading process, cracks gradually occurred in the shear section. The main crack kept propagating, with one end extending horizontally at the height where rebars were embedded and one end propagating diagonally to the loading point. Finally, the main crack penetrated the RC beam, leading to the beam’s failure. Besides, the location of the initial notch significantly affected the propagation of the main crack,

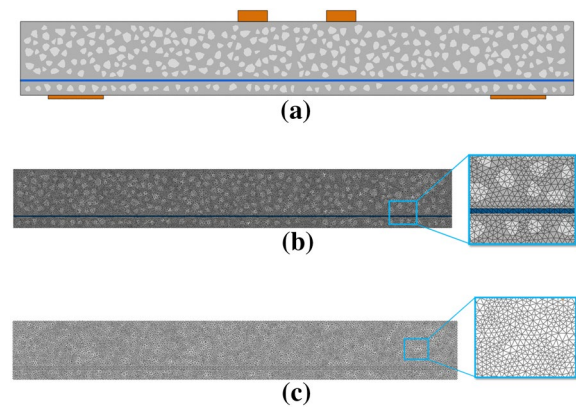


Fig. 16 Meso-model of the RC beam: **a** meso-model; **b** solid elements; **c** cohesive elements

as shown in Fig. 15d. The initial notch would induce the main crack closer to the midspan when the initial notch was near the midspan.

4 Numerical Analysis

4.1 Input Data of the Finite Element Model

Fig. 16 shows the meso-model of the RC beam designed in the FPB experiments. The volume ratio of the aggregate to concrete was set to 40%, and the particle size of aggregates was continually distributed in 5–20 mm. Due to the large size of the test beam and the limitation of the calculation efficiency, a size smaller than 10 mm aggregates were ignored in the model. The width of the rebar in the RC beam was set to 0.5ϕ . The thickness of the rebar and the corresponding rebar–concrete interface can be set to $0.5\pi\phi$. Thus, the section area of the rebar and the surface area of the rebar–concrete interface can be the same as the realistic one.

The mesh of the RC meso-model is shown in Fig. 16b–c. One typical model has about 70,000 nodes, 22,000 solid triangular elements, and 44,000 zero-thickness cohesive elements. The linear constitutive model was applied in all solid elements, and a part of cohesive elements (potential fracture surfaces of aggregate) since the aggregate was assumed undamaged. The constitutive models of potential fracture surfaces and rebar–concrete interfaces were implemented in the corresponding cohesive elements through the user-defined subroutine VUMAT based on the ABAQUS software (Simulia., 2014). The quasi-static method solved all the numerical models through the ABAQUS/EXPLICIT solver.

According to the experimental results, repeat trial computations, and related research (De Maio et al., 2019; Huang & Hu, 2019; López et al., 2008a, 2008b; Wang et al., 2015), the main material parameters

Table 2 Material parameters applied in the model

Element	k_n, k_s (GPa/m)	t_{n0} (MPa)	t_{s0} (MPa)	G_{n0} (N/m)	G_{s0} (N/m)	f
CE_MOR	10^6	2.50	8.75	100	1000	0.35
CE_ITZ	10^6	1.25	4.38	50	500	0.35
CE_AGG	10^6	–	–	–	–	–
CE_BOND	10^6	0.5	–	20	–	–

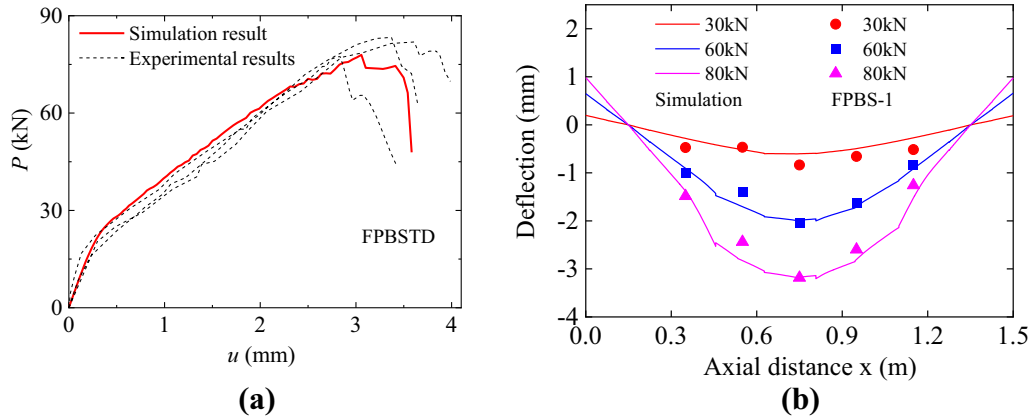


Fig. 17 Comparison between the simulation and experimental results in group FPBS: **a** P - u curves; **b** distribution of the deflection in different loading stage

applied in the cohesive elements are shown in Table 2. Besides, for solid elements of concrete, the elastic modulus of the mortar and aggregates were 25GPa and 50GPa, respectively, and the corresponding Poisson ratios were set to 0.22. For solid rebar elements, the elastic modulus, Poisson’s ratio, and yield strength were 200GPa, 0.3, and 400 MPa. For the bond–slip relation calculation of the rebar–concrete interface, the parameters were (Den Syroka-Korol et al., 2014; Uijl & Bigaj, 1996): $c_{eff} = 22$ mm, $f_t = 2$ MPa, $f_c = 40$ MPa, $E = 25$ GPa, $\phi = 10$ mm, $c_0 = 0.18$, $h_l = 0.5$ mm, $\psi = 0.2$.

4.2 Validation of the Numerical Model

Fig. 17 shows the comparisons between simulation and experimental results in group FPBS. The P - u curve obtained from the simulation shows a good agreement with the experimental results in curve shape and peak load. Also, the deflection distributions in different loading stages (30kN, 60kN, and 80kN) were extracted from the simulation result to compare with the experimental one (FPBS-1), as shown in Fig. 17b. The comparison results indicate that the proposed model can also well simulate the deflection evolution of the RC beams, no matter in the beginning or in the final stage of the loading process.

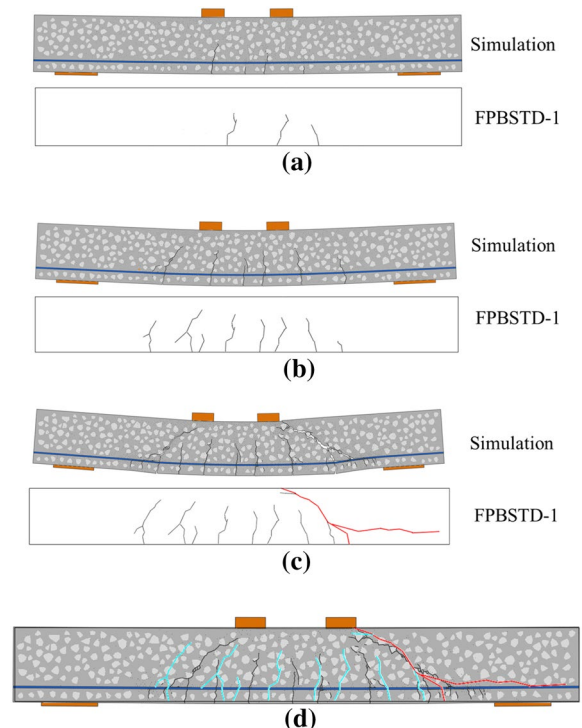


Fig. 18 Comparison of the crack distribution between simulation and experimental results in different loading stages: **a** 30kN; **b** 60kN; **c** failure stage; **d** comparison of the final crack distribution

To further validate the accuracy of the proposed meso-model, the crack distribution of the beam in different loading stages (30kN, 60kN, and final fracture stage) were also extracted and compared with the experimental one, as shown in Fig. 18. The cracks in the numerical model were represented by deleting the cohesive elements whose damage factor reached 1. The cracks first occurred in the pure-bending section of the beam. As the loading

proceeded, cracks gradually occurred in the shear section. Finally, the main crack penetrated the beam, with one end diagonally propagating to the loading point and one end extending horizontally. Through comparison, the evolution and propagation of the cracks obtained in the simulation results show a high similarity with the experimental results, especially for the main crack.

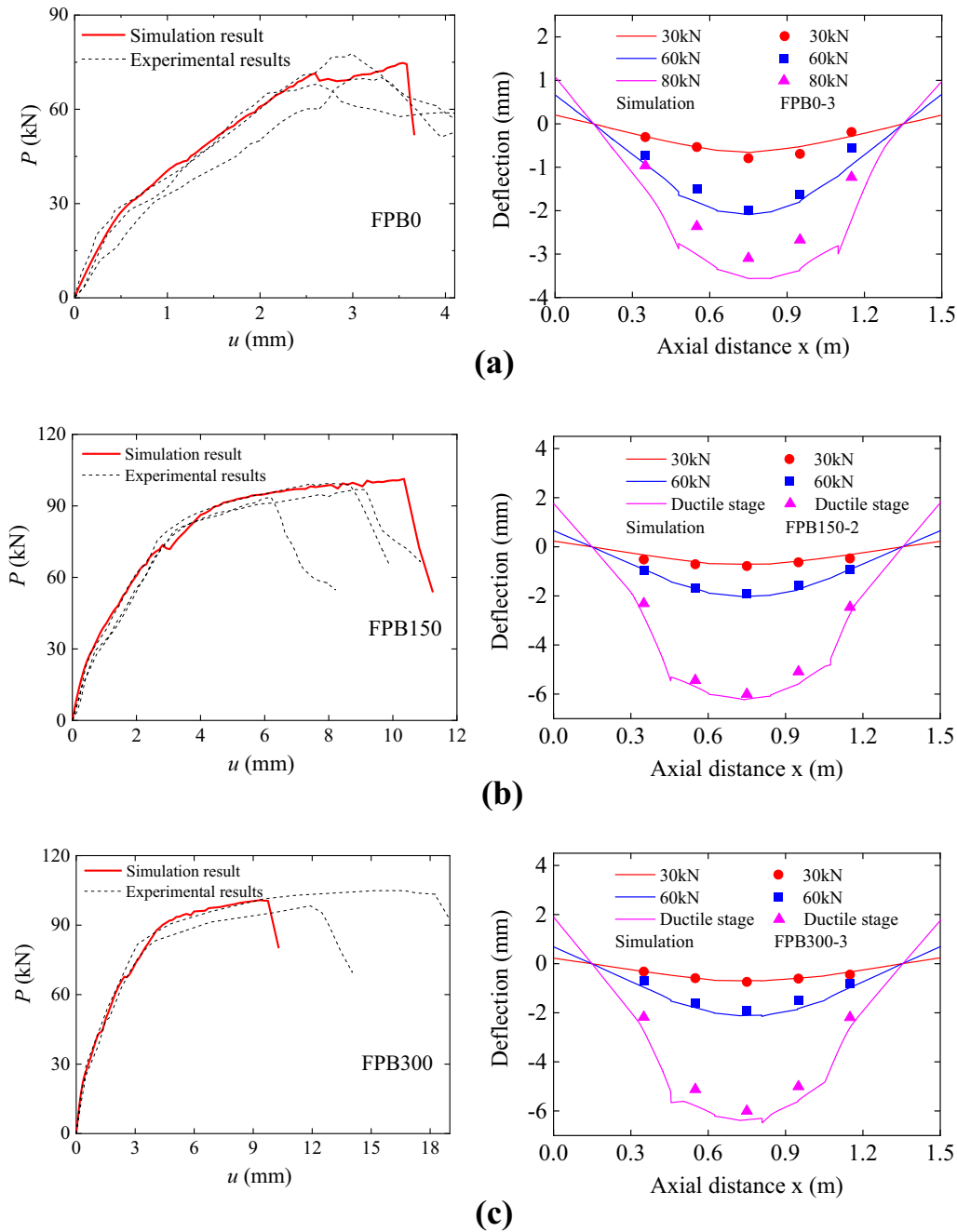


Fig. 19 *P*–*u* curves and the corresponding deflection distribution of RC beams: **a** FPB0; **b** FPB150; **c** FPB300

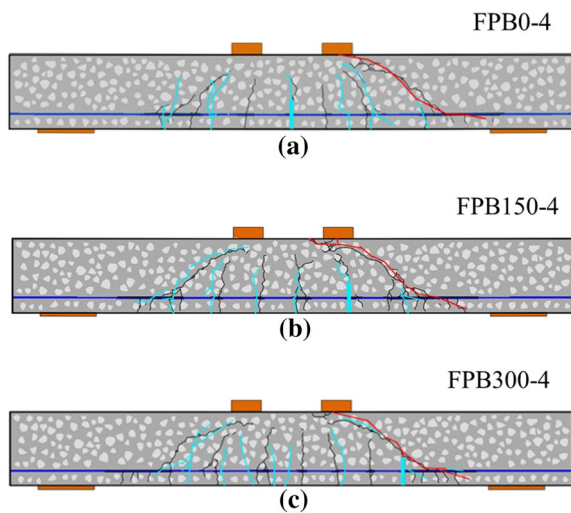


Fig. 20 Crack distribution of the beams extracted from simulation results and its comparisons with experimental results: **a** FPB0; **b** FPB150; **c** FPB300

The simulation P – u curves and deflection distributions of the beams with an initial notch are extracted in Fig. 19. The comparison results indicated that the proposed model not only can simulate the brittle fracture behavior of the RC beams but also can simulate the ductile fracture behavior of the beams. It should be noted that for the group FPB150 and FPB300, the deflection distribution of the beams in the ductile stage was compared. For the convenience of comparison and analysis, the deflection distribution at the state that midspan deflection is 6 mm extracted to reflect the deflection distribution in the ductile stage, as shown in Fig. 19b–c.

The crack distribution of the beams with initial notches in the failure stage was also extracted and compared with the experimental results, as shown in Fig. 20. No matter the brittle fracture or the ductile fracture, the crack distribution of the beams obtained from the simulation results all fitted well with the experimental ones, especially for the main crack. The initial notch's influence on the main crack's location was also reflected in the simulation results.

4.3 Comparison with Existing Rebar–Concrete Interface Constitutive Models

In the proposed model, the most significant difference compared with other research is that the rebar–concrete interface can be separated in the normal direction during the fracture process. For this reason, it is necessary to investigate the difference between the proposed constitutive model and the previous models. In previous studies, the most commonly used interface constitutive models

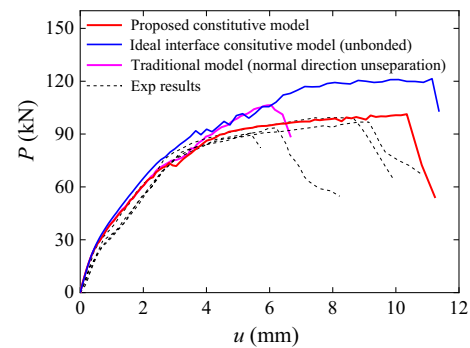


Fig. 21 Comparison between different interface constitutive models

were the ideal model (perfectly bonded) and the traditional constitutive model that only considered tangential evolution. Thus, in this section, these two constitutive models were adopted in the simulations to analyze with the proposed model. The beam in the group FPB150 was chosen as a typical model for analysis. Fig. 21 shows the comparison of the simulation results with different interface constitutive models. Regarding the ideal constitutive model, as the interface cannot separate in the normal direction and cannot slip tangentially, it can be seen that the stiffness, peak load, and the ductility of the RC beam was overestimated. Specifically, the peak load was overestimated by more than 20%, the peak load. As for the traditional constitutive model, due to the interface being allowed in the tangential direction, the stiffness and peak load of the beam is smaller than the one with ideal constitutive model. However, compared to the proposed model, the obtained result was still found to be overestimated (peak load was overestimated by about 10%), and the ductility of the RC beam was also not well simulated. In summary, when simulating the interfacial behavior of the rebar–concrete interface, the normal separation and the tangential slip should both be considered, or it may lead to an inaccurate result with overestimated bearing capacity and stiffness.

4.4 Energy Dissipation Analysis of the RC Beams

To further investigate the failure behavior of RC beams, a concrete energy analysis of the fracture process was carried out. FPBS and FPB150 beams were selected as typical beams because they exhibit brittle and plastic failure, respectively. In the proposed model, there are three types of energy dissipation that can be extracted from the zero-thickness cohesive elements (since all the fracture behavior was defined in these elements), and these parameters can be calculated as follows:

$$\begin{cases} E_n = th \int_l \left(\int_0^{\delta_n} t_n d\delta \right) dl, \\ E_s = th \int_l \left(\int_0^{\delta_s} (t_s - D \cdot T_f) d\delta \right) dl, \\ E_f = th \int_l \left(\int_0^{\delta_s} D T_f d\delta \right) dl \end{cases} \quad (22)$$

where E_n , E_s represent the energy dissipation in the normal and pure shear fracture process, respectively, and E_f represents energy dissipation due to friction; l represents the length of the zero-thickness cohesive element; th represents the out-of-plane thickness of the zero-thickness cohesive elements.

Fig. 22 shows the typical concrete internal energy dissipation of RC beams. Through the analysis of the $P-u$ curve, crack propagation pattern, and energy consumption pattern of each specimen, it can be observed that both brittle and ductile failures of the designed RC beams exhibit four typical stages during the failure process, as marked in Fig. 22. Also, to quantitatively and specifically

understand the energy consumption inside the concrete of beams, Table 3 lists the energy consumption of two typical specimens in each stage (Since there is almost no energy consumption in stage I, it is not listed). These four stage are

- (1) Stage I (elastic stage): the $P-u$ curve behaves as linear elastic, and almost no energy is consumed.
- (2) Stage II (tensile fracture stage): during this stage, the energy consumption in the normal direction is dominant (the energy consumption proportion of ΔE_n for beam FPBS and beam FPB150 are 88.30% and 86.86%, respectively), indicating that the failure mode in this stage is mainly Mode-I failure (tensile failure).
- (3) Stage III (shear fracture stage): in this stage, the proportion of energy dissipation from shear and friction increases significantly (The total proportion of tangential energy consumption ΔE_s and frictional energy consumption ΔE_f for beam FPBS and beam FPB150 are 66.02% and 47.74%, respectively), indicating that the failure mode has shifted from tensile failure to shear failure. In addition, the length of this

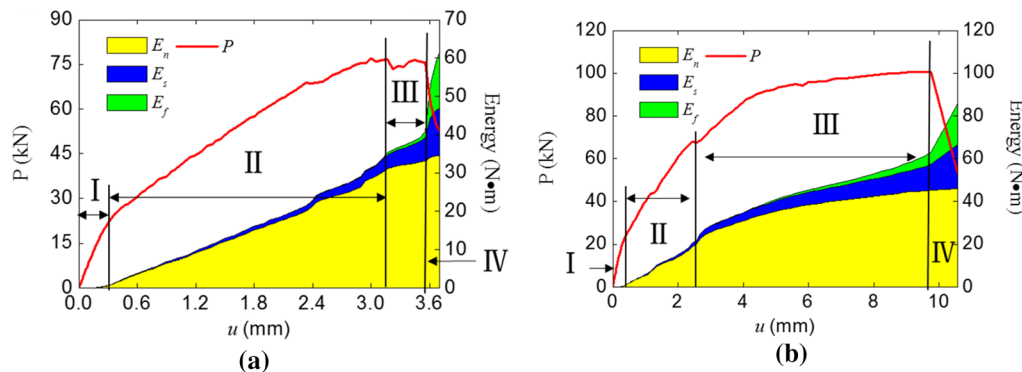


Fig. 22 Typical concrete internal energy dissipation of RC beams: **a** FPBS; **b** FPB150

Table 3 Energy consumption in each stage

Loading stage	Beam FPBS			Beam FPB150		
	Energy increment type	Energy value (N m)	Energy consumption proportion (%)	Energy increment type	Energy value (N m)	Energy consumption proportion (%)
Stage II	ΔE_n	30.56	88.30	ΔE_n	24.20	86.86
	ΔE_s	3.70	10.70	ΔE_s	3.41	12.24
	ΔE_f	0.35	1.00	ΔE_f	0.25	0.90
Stage III	ΔE_n	2.47	33.98	ΔE_n	19.77	52.26
	ΔE_s	2.95	40.58	ΔE_s	12.95	34.23
	ΔE_f	1.85	25.45	ΔE_f	5.11	13.51
Stage IV	ΔE_n	1.36	5.60	ΔE_n	1.35	4.09
	ΔE_s	5.80	23.88	ΔE_s	9.2	27.85
	ΔE_f	17.13	70.52	ΔE_f	22.49	68.07

stage determines whether the beam fails in a brittle or ductile manner.

- (4) Stage IV (failure stage): in the final stage, the specimen loses its bearing capacity, and the energy consumed by friction increases sharply (the proportion of frictional energy consumption ΔE_f for FPBS and FPB150 increased to 70.52% and 68.07%, respectively), indicating that significant slip and friction behavior has occurred inside the crack.

In summary, in the analysis of reinforced concrete structures, energy consumption can be used as an analysis indicator to determine their failure mode. In this analysis, the failure mode of the beam was initially tensile fracture and later shifted to shear fracture, and the ductility stage of the specimen was mainly characterized by shear fracture.

5 Conclusions

In this study, a meso-modeling method of RC structure was proposed. In the proposed meso-model, the cohesive elements were used to characterize the mechanical behavior of concrete potential fracture surfaces and the rebar–concrete interface. Based on the proposed model, the corresponding constitutive models were also developed. The constitutive model combined the mixed-mode bilinear damage relation and the friction effect for concrete potential fracture surfaces. For the rebar–concrete interface, the constitutive model determined the bond–slip relation by assuming the rebar as a cone, and the separation in the normal direction was especially considered. The constitutive models developed above were implemented through a user-defined subroutine in the FE software.

A series of four-point bending experiments were carried out to validate the proposed numerical model. The RC beams (without stirrups) with different initial notches were designed to obtain more fracture patterns. Analyzing the experimental results, the initial notch would influence the beams' failure mode (from the brittle fracture to the ductile fracture) and the corresponding crack distribution.

By comparing the simulation and experimental results, the proposed meso-model was proved to simulate the fracture behavior of the RC appropriately. Whether in the brittle fracture or ductile fracture condition, the load–displacement curves, deflection distribution, and crack distribution obtained from the simulation results can all fit well with the experimental ones.

Based on the proposed model, a comparison was made with existing models, and the failure mode of RC beams was analyzed based on energy dissipation, leading to the following conclusions:

1. By comparing the results of RC model without considering tangential sliding and normal separation, it was found that these constitutive models could lead to an overestimation of the bearing capacity (the peak load was overestimated by more than 10%) and stiffness of RC structures, and may result in computed ductility that does not match the actual behavior. Therefore, in the calculation of RC structures, it is necessary to consider both tangential slip and normal separation, as well as their coupling effect.
2. By analyzing the energy consumption of the RC beam during the fracture process, it was found that there were changes in energy dissipation during the beam's failure process (the proportion of energy consumption in tensile failure changes from approximately 86% to 89% to approximately 43% to 52%), indicating a transition in the failure mode from initial tensile failure to gradually shear failure. This demonstrates that the proposed model can not only be used to characterize the failure process of the beam but also quantitatively analyze the composition of internal failure modes.

Acknowledgements

The authors wish to express their gratitude to the Natural Science Foundation of Fujian Province with the research number 2022J01931 and the Research Development Fund project of Fujian University of Technology with research number GY-Z18185.

Author contributions

Conceptualization, investigation, data curation, methodology, writing—original draft, writing—review, and funding acquisition: ZLW; writing—original draft, writing—review, formal analysis, funding acquisition, and supervision: WZ; investigation, data curation, methodology, writing—original draft, and writing—review: YQH. All authors read and approved the final manuscript.

Authors' information

Zhanliang Wang is an assistant professor at Fujian University of Technology, Fuzhou, China.

Wei Zhang is a professor at Fujian University of Technology, Fuzhou, China.

Yiqun Huang is an assistant professor at Fujian University of Technology, Fuzhou, China.

Funding

This research was funded by the Natural Science Foundation of Fujian Province with the research number 2022J01931 and the Research Development Fund project of Fujian University of Technology with research number GY-Z18185.

Availability of data and materials

All data generated or analyzed during this study are included in this published article.

Declarations

Competing interests

No competing interests exist in the submission of this manuscript, and the manuscript has been approved by all authors for publication. The author declares that the work described is original research that has not been published previously and is not under consideration for publication elsewhere, in whole or in part.

Received: 9 January 2023 Accepted: 22 April 2023

Published online: 01 August 2023

References

- Bernachy-Barbe, F., & Bary, B. (2019). Effect of aggregate shapes on local fields in 3D mesoscale simulations of the concrete creep behavior. *Finite Elements in Analysis and Design*, 156, 13–23.
- Chaudhuri, P. (2013). Multi-scale modeling of fracture in concrete composites. *Composites Part B: Engineering*, 47, 162–172.
- Chen, H., Xu, B., Wang, J., Nie, X., & Mo, Y. (2020). XFEM-based multiscale simulation on monotonic and hysteretic behavior of reinforced-concrete columns. *Applied Sciences*, 10(21), 7899.
- Cox, J. V., & Herrmann, L. R. (1998). Development of a plasticity bond model for steel reinforcement. *Mechanics of Cohesive-Frictional Materials: An International Journal on Experiments, Modelling and Computation of Materials and Structures*, 3(2), 155–180.
- De Maio, U., Fabbrocino, F., Greco, F., Leonetti, L., & Lonetti, P. (2019). A study of concrete cover separation failure in FRP-plated RC beams via an inter-element fracture approach. *Composite Structures*, 212, 625–636.
- De Maio, U., Greco, F., Leonetti, L., Blasi, P. N., & Pranno, A. (2022). An investigation about debonding mechanisms in FRP-strengthened RC structural elements by using a cohesive/volumetric modeling technique. *Theoretical and Applied Fracture Mechanics*, 117, 103199.
- Den Uijl, J. A., & Bigaj, A. J. (1996). A bond model for ribbed bars based on concrete confinement. *HERON*, 41(3), 1996.
- Deng, X., Liang, S., Fu, F., & Qian, K. (2020). Effects of high-strength concrete on progressive collapse resistance of reinforced concrete frame. *Journal of Structural Engineering*, 146(6), 4020078.
- Du, X., Jin, L., & Ma, G. (2013). A meso-scale analysis method for the simulation of nonlinear damage and failure behavior of reinforced concrete members. *International Journal of Damage Mechanics*, 22(6), 878–904.
- Fan, W., Zhong, Z., Huang, X., Sun, W., & Mao, W. (2022). Multi-platform simulation of reinforced concrete structures under impact loading. *Engineering Structures*, 266, 114523.
- Grassi, P. (2022). 3D lattice meso-scale modelling of the effect of lateral compression on tensile fracture processes in concrete. *International Journal of Solids and Structures*, 262–263, 112086.
- Huang, Y., & Hu, S. (2019). A cohesive model for concrete mesostructure considering friction effect between cracks. *Computers and Concrete an International Journal*, 24(1), 51–61.
- Huang, Y., Zhang, W., & Liu, X. (2022). Assessment of diagonal macrocrack-induced debonding mechanisms in FRP-strengthened RC beams. *Journal of Composites for Construction*, 26(5), 4022056.
- Jeong, C., Kim, H., Kim, S., Lee, K., & Kim, K. (2017). Size effect on shear strength of reinforced concrete beams with tension reinforcement ratio. *Advances in Structural Engineering*, 20(4), 582–594.
- Jin, L., Liu, M., Zhang, R., & Du, X. (2020). 3D meso-scale modelling of the interface behavior between ribbed steel bar and concrete. *Engineering Fracture Mechanics*, 239, 107291.
- Karavelić, E., Nikolić, M., Ibrahimbegovic, A., & Kurtović, A. (2019). Concrete meso-scale model with full set of 3D failure modes with random distribution of aggregate and cement phase. Part I: Formulation and numerical implementation. *Computer Methods in Applied Mechanics and Engineering*, 344, 1051–1072.
- Li, X., & Wu, G. (2018). Finite-element analysis and strength model for IC debonding in FRP-strengthened RC beams. *Journal of Composites for Construction*, 22(5), 4018030.
- Liu, J., Wenxuan, Y., Xiuli, D. U., Zhang, S., & Dong, L. I. (2019). Meso-scale modeling of the size effect on dynamic compressive failure of concrete under different strain rates. *International Journal of Impact Engineering*, 125, 1–12.
- Liu, M., Jin, L., Chen, F., Zhang, R., & Du, X. (2022). 3D meso-scale modelling of the bonding failure between corroded ribbed steel bar and concrete. *Engineering Structures*, 256, 113939.
- López, C. M., Carol, I., & Aguado, A. (2008a). Meso-structural study of concrete fracture using interface elements. I: numerical model and tensile behavior. *Materials and Structures*, 41(3), 583–599.
- López, C. M., Carol, I., & Aguado, A. (2008b). Meso-structural study of concrete fracture using interface elements. II: compression, biaxial and Brazilian test. *Materials and Structures*, 41(3), 601–620.
- Murthy, A. R., Karihaloo, B. L., & Priya, D. S. (2018). Flexural behavior of RC beams retrofitted with ultra-high strength concrete. *Construction and Building Materials*, 175, 815–824.
- Naderi, S., & Zhang, M. (2021). Meso-scale modelling of static and dynamic tensile fracture of concrete accounting for real-shape aggregates. *Cement and Concrete Composites*, 116, 103889.
- Ooi, E. T., & Yang, Z. J. (2011). Modelling crack propagation in reinforced concrete using a hybrid finite element-scaled boundary finite element method. *Engineering Fracture Mechanics*, 78(2), 252–273.
- Pedersen, R. R., Simone, A., & Sluys, L. J. (2013). Mesoscopic modeling and simulation of the dynamic tensile behavior of concrete. *Cement and Concrete Research*, 50, 74–87.
- Roth, S., Léger, P., & Soulaïmani, A. (2015). A combined XFEM–damage mechanics approach for concrete crack propagation. *Computer Methods in Applied Mechanics and Engineering*, 283, 923–955.
- Shen, L., Ren, Q., Xia, N., Sun, L., & Xia, X. (2015). Mesoscopic numerical simulation of effective thermal conductivity of tensile cracked concrete. *Construction and Building Materials*, 95, 467–475.
- Simulia. (2014). Abaqus analysis user's guide, version 6.14: Dassault Systemes Providence, RI
- Sun, B., Huang, X., Zheng, Y., & Guo, L. (2020). Multi-scale lattice method for mesoscopic crack growth simulation of concrete structures. *Theoretical and Applied Fracture Mechanics*, 106, 102475.
- Syroka-Korol, E., & Tejchman, J. (2014). Experimental investigations of size effect in reinforced concrete beams failing by shear. *Engineering Structures*, 58, 63–78.
- Syroka-Korol, E., Tejchman, J., & Mróz, Z. (2014). FE analysis of size effects in reinforced concrete beams without shear reinforcement based on stochastic elasto-plasticity with non-local softening. *Finite Elements in Analysis and Design*, 88, 25–41.
- Wang, X. F., Yang, Z. J., Yates, J. R., Jivkov, A. P., & Zhang, C. (2015). Monte Carlo simulations of mesoscale fracture modelling of concrete with random aggregates and pores. *Construction and Building Materials*, 75, 35–45.
- Xia, X., Chen, F., Gu, X., Fang, N., & Zhang, Q. (2021). Interfacial debonding constitutive model and XFEM simulation for mesoscale concrete. *Computers & Structures*, 242, 106373.
- Yang, Z., Ren, W., Sharma, R., McDonald, S., Mostafavi, M., Vertyagina, Y., & Marrow, T. J. (2017). In-situ X-ray computed tomography characterisation of 3D fracture evolution and image-based numerical homogenisation of concrete. *Cement and Concrete Composites*, 75, 74–83.

Publisher's Note

Springer Nature remains neutral with regard to jurisdictional claims in published maps and institutional affiliations.